



Graphene-wrapped Pt/TiO₂ photocatalysts with enhanced photogenerated charges separation and reactant adsorption for high selective photoreduction of CO₂ to CH₄



Yilong Zhao^{a,1}, Yuechang Wei^{a,*1}, Xingxing Wu^a, Huiling Zheng^a, Zhen Zhao^{a,b,*}, Jian Liu^{a,*}, Jianmei Li^a

^a State Key Laboratory of Heavy Oil Processing, College of Science, China University of Petroleum, Beijing, 102249, China

^b Institute of Catalysis for Energy and Environment, Shenyang Normal University, Shenyang, 110034, China

ARTICLE INFO

Keywords:

TiO₂ nanocrystal
Graphene sheets
Pt nanoparticles
Core-shell structure
Photocatalytic CO₂ reduction

ABSTRACT

Artificial photosynthesis efficiency for selective CO₂ conversion to CH₄ as chemical energy-rich molecule is dependent on the photogenerated charges separation and reactant adsorption property of photocatalyst. Here we report a novel fabrication of core-shell-structured photocatalysts of Pt/TiO₂-nanocrystals wrapped by reduced graphene oxide (rGO) sheets ((Pt/TiO₂)@rGO). The ultrafine anatase TiO₂ nanocrystals with coexposed {001} and {101} facets acted as the fountain of the photogenerated charges primitively. Pt nanoparticles (NPs) deposited on the TiO₂ nanocrystals can gather and transfer the stimulated electrons originated from anatase TiO₂ nanocrystals. The all-solid-state electron multiple transmission (EMT) system with TiO₂-nanocrystal(core)-Pt (mediator)-rGO(shell) nanojunction is not only favorable to the vectorial electron transfer of TiO₂ → Pt → rGO and enhance the separation efficiency of photogenerated electrons and holes, but also the surface residual hydroxyl and extended π bond of wrapping rGO sheets can improve the adsorption and activation capabilities for CO₂ reactant. (Pt/TiO₂)@rGO ternary photocatalysts exhibit excellent performance for the multi-electron process of selective photocatalytic CO₂ conversion to CH₄. Among the prepared catalysts, (Pt/TiO₂)@rGO-2 catalyst shows the highest photocatalytic activity and selectivity for CO₂ conversion, i.e., the formation rate of CH₄ is 41.3 μmol g⁻¹ h⁻¹ and the selectivity of CO₂ conversion to CH₄ product is 99.1%, and its apparent quantum efficiency for CH₄ product is 1.93%. As a heuristic the fabrication of core-shell structured (Pt/TiO₂)@rGO photocatalysts will stimulate more novel ideas for application to light-chemical energy conversion.

1. Introduction

Global climate change caused by the rapid growth of carbon dioxide (CO₂) concentrations in our atmosphere is regarded as one of the greatest crises in this century [1,2]. Scientists have long dreamed of mimicking photosynthesis of green plants, by using the energy in sunlight to knit together hydrocarbon fuels from water and CO₂, the chief culprit in global warming [3,4]. Since the pioneering researches reported by Fujishima [5], a variety of high efficient semiconductor-based photocatalysts with the suitable band gap for CO₂ reduction with H₂O have been reported [6–10]. However, practical applications of photocatalytic reduction of CO₂ are limited because of the low selectivity of reductive production and the low fuel-conversion efficiency caused by the rapid recombination of photogenerated electrons and holes. Therefore, the design and synthesis of efficient photocatalysts to

decrease the recombination of photogenerated charge carriers and/or enhancing the selectivity and activity of reduction products have attracted much attention in global [11,12].

Among the previous reported photocatalysts, TiO₂ is the most widely applied semiconductor materials because of its nontoxicity, long-term stability, corrosion resistant and cost inexpensive [13–17]. The catalytic activities of TiO₂-based materials for photocatalysis are related to the exposed low-index facets of {001}, {010} and {101} with the average surface energies of 0.90, 0.53 and 0.44 J m⁻² in single anatase nanocrystals, respectively [18]. The role of {101} facet is the selective gathering of surface photogenerated electrons, while surface photogenerated holes remain on the surface of {001} facet, because of their different the electronic energy levels and the distribution of potential trapping sites [19]. Thus, the coexposed {101} and {001} facets on a single anatase TiO₂ nanocrystal can form a surface heterojunction,

* Corresponding authors at: 18# Fuxue Road, Chang Ping District, Beijing, 102249, China.

E-mail addresses: weiyc@cup.edu.cn (Y. Wei), zhenzhao@cup.edu.cn (Z. Zhao), liujian@cup.edu.cn (J. Liu).

¹ Yilong Zhao and Yuechang Wei contributed equally to this work.

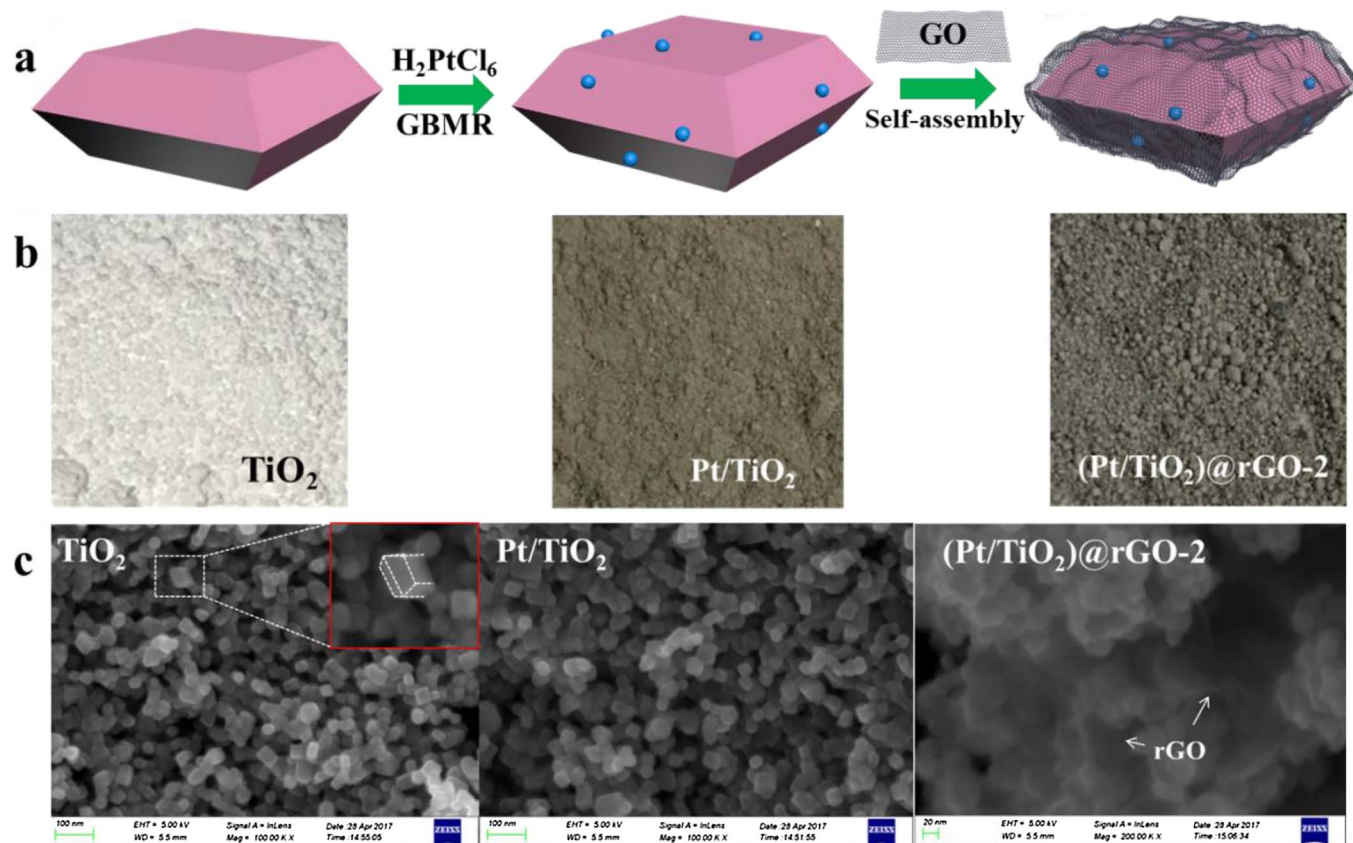


Fig. 1. The schematic for the two step synthesis of supported Pt NPs and wrapping rGO shells on the surface of TiO_2 nanocrystals (a). The digital photograph (b) and SEM images (c) of TiO_2 , Pt/TiO_2 and $(\text{Pt}/\text{TiO}_2)@\text{rGO-2}$ catalysts.

which is favorable to the separation of photogenerated charges. Anatase TiO_2 nanocrystals with an optimal percentage of $\{101\}$ and $\{001\}$ facets can further improve separation of photogenerated carriers and enhance photocatalytic activity [20], and the ultrafine TiO_2 nanocrystals with small size and large surface area can further improve the photocatalytic activity for CO_2 reduction to methane (CH_4) due to the increasing active sites on the surface of crystal facets heterojunction [21]. However, the photocatalytic activity of single TiO_2 nanocrystal for CO_2 reduction is not efficient enough to the industrialized application because of the low selectivity and production rate, which is related to the rapid recombination of photogenerated charges and the insufficient surface adsorption sites for CO_2 and H_2O [22–24].

Based on the reaction nature of the photocatalytic CO_2 reduction with H_2O , the product of one CH_4 molecule requires eight electrons, eight hydrogen protons and one CO_2 molecule. Thus, the surface enrichments of photogenerated electrons and adsorbed reactant molecules are very critical for improving formation rate and selectivity of CH_4 product [25]. It is generally strategy that supported noble metal nanoparticles (NPs) could suppress the recombination of photogenerated charges and improve the utilization efficiency of photogenerated electrons [26–29]. Due to the Fermi levels of Pt NPs below the conduction band edge of TiO_2 energetically, photogenerated electrons in the conduction band (CB) of TiO_2 can be rapidly transferred and trapped on the surface of supported Pt NPs as a reservoir of photoelectrons [30,31]. Thus, supported Pt NPs as electron trap are beneficial to improve photogenerated charge separation and photocatalytic activity, especially to the formation of H_2 product from water splitting via bi-electron reduction process. However, the improving selectivity of CH_4 product is still a challenge due to its low capability of adsorption and activation for CO_2 reactant.

Recently, the graphene materials can play important roles in improving the photocatalytic performance, including co-catalyst [32,33],

photosensitizer [34,35], coupler [36,37] and photocatalysts [38–43]. It has been demonstrated that graphene as a high-efficiency acceptor and transporter of electron is potential to further improve the separation efficiency of photogenerated electrons and holes in artificial photosynthesis reaction [44–47]. Moreover, the graphene oxide materials with the surface hydroxyl and extended π bond can enhance the adsorption and activation capacity for CO_2 and H_2O molecules. Integrating the above preeminent properties, the construction of rGO-Pt- TiO_2 ternary nanojunction combined with optimal percent of coexposed $\{001\}$ and $\{101\}$ facets is expected to bring high properties and new revolution for photocatalytic CO_2 reduction.

Herein, the core-shell-structured photocatalysts of Pt/TiO_2 nanocrystals wrapped by reduced graphene oxide (rGO) ultrathin sheets ($(\text{Pt}/\text{TiO}_2)@\text{rGO}$) were synthesized by a self-assembly method of a simple and pure chemical bonding reactions. The core part of well-defined core-shell structure is the truncated octahedral bipyramid anatase TiO_2 nanocrystal with optimized proportion of coexposed $\{001\}$ -51% and $\{101\}$ -49% facets for photogenerated charges separation. The all-solid-state electron multiple transmission system with TiO_2 (core)-Pt(mediator)-rGO(shell) nanojunction can achieve the high-efficiency separation of photogenerated electrons and holes via the two-step vectorial electron transfer of $\text{TiO}_2 \rightarrow \text{Pt} \rightarrow \text{rGO}$, which exhibits ternary system far exceeding the unitary or binary systems. It suggests that $(\text{Pt}/\text{TiO}_2)@\text{rGO}$ catalysts are an excellent system not only for surface chemical processes occurred at the interfaces of reactant and catalyst, but also for light-chemical energy conversion.

2. Experimental section

2.1. Sample preparation

The core-shell-structured $(\text{Pt}/\text{TiO}_2)@\text{rGO}$ photocatalysts were

designed and practical fabricated by a self-assembly method of a simple and pure chemical bonding reactions (detailed in the *Supplementary Information of Sample Preparation*), and the schematic representation and digital photographs of the preparation processing for (Pt/TiO₂)@rGO core-shell photocatalysts are shown in Fig. 1. As shown in Fig. 1a, the typical procedures with three steps were described as follows: Firstly, the truncated octahedral bipyramid anatase TiO₂ nanocrystal with coexposed {001}-51% and {101}-49% facets were synthesized by two steps of hydrothermal processes using commercial P25 as Ti source reported by Cao et al. [21]. As shown in Fig. 1b of digital photographs, anatase TiO₂ nanocrystal with white color was obtained after washed, dried and calcined processes. Secondly, Pt NPs supported on anatase TiO₂ nanocrystals were prepared by the gas bubbling-assisted membrane reduction (GBMR) method using the poly (N-vinyl-2-pyrrolidone) (PVP) as the protecting agent and the NaBH₄ solution as the reducing agent (Fig. S1). The GBMR process can control the nucleation and growth processes of Pt nucleus on the surface of anatase TiO₂ nanocrystals via highly homogeneous dispersion of reductant using the ceramic membrane tubes. And it is also critical process that [PtCl₆]²⁻ ions are adsorbed and anchored on surface [OH₂]⁺ groups of anatase TiO₂ nanocrystals, because the pH value of mixture solution (~3.0) using the adjustment of HCl solution is lower than the isoelectric point (IEP) of TiO₂. After supported Pt NPs, the color of samples changed from white to light gray in Fig. 1b. The loading amounts of supported Pt NPs in the photocatalyst is 1.0 wt% in theory. Thirdly, the core-shell-structured photocatalysts of Pt/TiO₂ nanocrystals wrapped by rGO sheets were synthesized by a self-assembly method of a simple and pure chemical bonding reactions. Graphite oxide (GO) was prepared by the traditional Hummers method from graphite power (Fig. S2), and the exfoliated GO shows super electronic conductivity because of the π -system interruption by substitution with a numerous defects (oxygen functional groups) [48], thus, GO dispersed in ethyl alcohol are strongly adsorbed on the surface of Pt/TiO₂ nanocrystals due to surface condensation reaction of oxygen-containing functional groups. Then, GO/(Pt/TiO₂) samples were reduced to rGO using NaBH₄ solutions [49]. Finally, the desired core-shell structured (Pt/TiO₂)@rGO catalysts with dark gray (Fig. 1b) were obtained after centrifugation, wash and dry in a vacuum oven at 60 °C for 12 h. The catalysts are uniformly named as (Pt/TiO₂)@rGO-n, where n is the nominal weight percent of rGO to Pt/TiO₂ (1, 2, 5 and 10 wt% of Pt/TiO₂).

2.2. Characterization

The morphology and microscopic structure information were obtained on a scanning electron microscope (SEM, FEI Quanta 200F) and a transmission electron microscope (TEM, JEOL JEM 2100) equipped with a field emission source at an accelerating voltage of 200 kV. The nitrogen adsorption/desorption isotherm was carried out at -196 °C by using an automated gas sorption analyzer (Quantachrome Autosorb-iQ, USA) after having degassed the sample for 4 h at 300 °C. The specific surface area was calculated by the Brunauer-Emmett-Teller (BET) method. The crystal phase properties of all as-prepared samples were analyzed with a powder X-ray diffractometer (Shimadzu XRD 6000) and a Renishaw Micro-Raman System 2000 spectrometer. The laser line of Raman microscope was 532 nm. X-ray photoelectron spectra (XPS) were acquired by a Perkin-Elmer PHI-1600 ESCA spectrometer with Mg Ka emission. Photoluminescence (PL) spectra were recorded using the Edinburgh Instruments Xe900 equipped with a Xe lamp and the excitation wavelength was set at 380 nm. Photoelectrochemical (PEC) measurements were performed on an electrochemical workstation (CHI660E) in the saturated solution of Na₂SO₄, which has a three-electrode configuration and all as-prepared samples, the saturated Ag/AgCl, a platinum foil were employed to as working photoelectrode, reference and counter electrode, respectively. The samples were illuminated under a 300 W Xe lamp. Temperature-programmed desorption of carbon dioxide (CO₂-TPD) measurement was performed on a

conventional flow apparatus. Prior to measurements, 100 mg of the sample was pretreated in Ar gas (60 cm³ min⁻¹) at 150 °C for 1 h and then cooled down to room temperature. Next, the sample was exposed to CO₂ flow of 30 cm³ min⁻¹ for 0.5 h to ensure the sufficient adsorption of CO₂. Before desorption, the sample was flushed in Ar gas for 1 h. Subsequently, CO₂ desorption was performed in the range of 30–400 °C at a heating rate of 10 °C min⁻¹ under an Ar flow of 30 cm³ min⁻¹. In-situ diffuse reflectance Fourier transform infrared spectroscopy (DRIFTS) were recorded using a thermo Nicolet IS50 spectrometer, which was equipped with a high temperature environmental cell fitted with Zn-Se window and an MCT detector cooled with liquid N₂. The catalyst was loaded in the Harrick IR cell and heated to 200 °C under N₂ at a flow rate of 50 cm³ min⁻¹ for 60 min to remove adsorbed impurities. Then the catalyst was cooled down to 30 °C. A background spectrum was collected under a flowing N₂ atmosphere and was subtracted from the sample spectra. Next, the sample was exposed to CO₂ flow of 50 cm³ min⁻¹ for 30 min and then under N₂ at a flow rate of 50 cm³ min⁻¹ for 30 min. The in-situ DRIFTS spectra were recorded by accumulating 64 scans with a resolution of 4 cm⁻¹. Density functional theory (DFT) calculation was carried out by the Vienna ab initio simulation package (VASP) in order to elucidate relationship between the origin of visible absorption and oxygen defects. The calculations involved on-site Coulomb corrections (DFT + U, U = 4.2 eV for Ti 3d states). [50] PAW pseudopotential was used to describe the core-valence electron interaction. Plane-wave basis set with an energy cutoff of 400 eV was used in this work. Anatase TiO₂ (001) facet was presented by a five-layer slab model with a vacuum gap of 15 Å. For all the surface calculations, the model was a periodic slab with a (2 × 2) surface unit cell. A Monkhorst pack 6 × 6 × 1 k-point mesh was used for the Brillouin zone integration. During structural optimizations, all of the atoms except those in the bottom TiO₂ two layers of the slab were allowed to relax until atom forces were smaller than 0.05 eV Å⁻¹.

2.3. Photocatalytic reduction of CO₂ with H₂O test

Photocatalytic CO₂ reduction test was carried out in a gas-closed circulation system (Perfect Light Company, Beijing, China) irradiated under a 300 W Xe lamp (320–780 nm). The certain amount of catalysts was uniformly dispersed on a watch-glass with 6.5 cm basal diameter. Before the light irradiation, the photo reactor system was thoroughly vacuum-treated, then CO₂ gas was introduced into the circulation system. The deionized water (2 mL) was injected into the bottom of the reactor. The intensity of incident light was measured to be 80 mW cm⁻² by a spectroradiometer. During the light irradiation in 8 h, the amounts of H₂, CO, and hydrocarbons in the reactor were analyzed by an online gas chromatograph (GC-9560; HuaAiSePu Corp., Shanghai, China) with a flame ionization detector (FID) and a thermal conductivity detector (TCD) each 60 min intervals. The gas products were analyzed by the external standard method. The apparent quantum efficiency (AQE) was measured under the similar photocatalytic reaction condition, and the irradiation light (wavelength 380 nm) using a band-pass filter (full width at half maximum 15 nm) was used as the light source. The incident flux was determined by Radiometer (FZ-A, Photoelectric Instrument Factory of Beijing Normal University). The AQE values for CH₄ evolution of CO₂ reduction were calculated according to the following equation:

$$\Phi\text{CH}_4 (\%) = \frac{8 \times [\text{the number of evolved CH}_4 \text{ moleculars}]}{[\text{number of incident photons}]} \times 100\%$$

3. Results

3.1. The characterization results of the catalysts

Fig. 1 shows the schematic, digital photographs and SEM images for synthesis procedures of (Pt/TiO₂)@rGO-n catalysts. With progressing of

the preparation process, the color of prepared samples has changed obviously from white to light gray and even dark gray in Fig. 1b. It indicates that the surface of anatase TiO_2 nanocrystals with white color are deposited successively by Pt NPs and rGO sheets with black color. As shown in Fig. 1c of SEM images, pure anatase TiO_2 nanocrystals show the homogeneously truncated octahedral bipyramidal structure with bare surface clearly. The average particle size of TiO_2 nanocrystals is 30 nm estimated by counting more than 100 nanoparticles. And the truncated octahedral bipyramidal nanostructure of TiO_2 nanocrystal is not influenced by supported Pt nanoparticles via the synthesis process of GBMR method. After further introduction of rGO sheets, the truncated octahedral bipyramidal morphology is obscured, and the Pt/TiO_2 -wrapped ultrathin rGO nanolayer catalysts present a wrinkle-like morphology uniformly, indicating that the core-shell structure of Pt/TiO_2 nanocrystals wrapped by rGO sheets can be obtained by a pure chemical bonding reaction successfully. With increasing of the mass ratios of rGO/ TiO_2 , the surface feature of truncated octahedral bipyramidal nanocrystals become indistinct and even disappear due to the excess wrapped by rGO sheets (Fig. S3).

The phase structures of TiO_2 , Pt/TiO_2 , $\text{TiO}_2@r\text{GO-2}$ and $(\text{Pt}/\text{TiO}_2)@r\text{GO-n}$ catalysts were investigated by XRD patterns and the results are shown in Fig. 2. The diffraction peaks (20) of TiO_2 nanocrystals at 25.3, 37.8, 48.0, 53.9, 55.1, 62.7 and 75.0° can be indexed to the (101), (004), (200), (105), (211), (204) and (215) crystal facets of anatase-phase TiO_2 (PDF# 21-1272), respectively. There is not any diffraction peak corresponding to other phase of TiO_2 , indicating that the phase structure of anatase TiO_2 nanocrystal is single and pure. After introduction of supported Pt NPs, the diffraction peaks belonging to TiO_2 did not change, and the characteristic diffraction peaks of Pt NPs were not detected. The above-mentioned results indicate that the sizes or loadings of supported Pt NPs are smaller than the detection limit of XRD spectra for supported nanoparticles. Meanwhile, no diffraction peaks for carbon species were observed in $\text{TiO}_2@r\text{GO}$ and $(\text{Pt}/\text{TiO}_2)@r\text{GO}$ samples, which might be due to the relatively low diffraction intensity of graphene. No obvious change of its crystalline phase is observed after Pt NPs deposited and rGO sheets coated on TiO_2 nanoparticles. In addition, Table S1 shows the structural physical parameters of TiO_2 , Pt/TiO_2 , $\text{TiO}_2@r\text{GO-2}$ and $(\text{Pt}/\text{TiO}_2)@r\text{GO-n}$ catalysts including surface areas, pore volumes, crystal parameters and Pt actual contents. After introduction of supported Pt NPs and wrapping rGO sheets, the surface areas and pore volumes of the catalysts have not changed obviously, and the Pt actual contents in the catalysts determined by ICP-AES are always in the range of 0.8–0.9 wt%.

Raman spectroscopy is an excellent characterization technique to further observe the phase structure of TiO_2 and rGO sheets owing to its strong scattering properties. As shown in Fig. 3, Raman spectra of all the samples show several characterized bands located at 144, 397, 517, and 638 cm^{-1} , which is assigned to the $E_{\text{g}(1)}$, $B_{1\text{g}(1)}$, $A_{1\text{g}}$ + $B_{1\text{g}(2)}$, and

$E_{\text{g}(2)}$ modes of anatase phase of TiO_2 , respectively [51]. The single anatase phase structure of TiO_2 support is further confirmed. After introduction of wrapping rGO nanolayers, it is worth noting that two typical bands centered at 1347 and 1590 cm^{-1} are observed obviously, which is assigned to the D-band and G-band of the graphitized structure of rGO sheets, respectively. With the increasing of wrapping rGO contents, the intensity of the characteristic bands of anatase TiO_2 nanocrystals decreases gradually and even disappears for the $(\text{Pt}/\text{TiO}_2)@r\text{GO-10}$ catalyst, which is direct evidence of $(\text{Pt}/\text{TiO}_2)@r\text{GO}$ core-shell structure. On the other hand, with the increasing of RGO content, the thickness of rGO in the core-shell structure grows larger gradually.

In order to further investigate the physical structure, TEM and HRTEM images of TiO_2 , Pt/TiO_2 and $(\text{Pt}/\text{TiO}_2)@r\text{GO-n}$ catalysts are shown in Fig. 4. For TiO_2 nanocrystals, the hexagons as projection of truncated octahedral bipyramidal are exhibited. The lateral isosceles trapezoid of the truncated octahedral bipyramidal nanocrystals corresponds to the $\{101\}$ facet, and the top and bottom facets are the $\{001\}$ facet [52]. The interfacial angle between $\{101\}$ and $\{001\}$ facets is 68.3° . The mean particle size of anatase TiO_2 nanocrystal is about 30 nm in accordance with SEM results. As shown in inset of Fig. 4a, the lattice spacings paralleled to the lateral and the top faces are ca. 0.35 and 0.24 nm, which are corresponding to the $\{101\}$ and $\{004\}$ facets of anatase TiO_2 , respectively. Anatase TiO_2 nanocrystal was estimated to be coexposed $\{001\}$ -51% and $\{101\}$ -49% facets as calculated by a reported method [53]. The coexposed $\{101\}$ and $\{001\}$ facets on a single anatase TiO_2 nanocrystal can form a surface heterojunction owing to different surface energy and band edge positions, which are favorable for the separation of photogenerated carriers. For Pt/TiO_2 catalysts, a mass of bare Pt NPs supported on the surface of TiO_2 nanocrystals can be clearly observed in Fig. 4b, and the average diameter of Pt NPs with a narrow distribution is 3.3 nm. As shown in inset of Fig. 4b, the lattice fringes (0.22 nm) of one hemispherical Pt NP exhibit clearly the exposed $\{111\}$ facet, and the crystal fusion domain at the phase interface of Pt-TiO_2 shows a strong lattice distortion. It indicates that there is a tight contact interface between Pt NPs and TiO_2 nanocrystals, which is beneficial to the subsequent efficient electron transfer and rGO shell coating.

After introduction of rGO sheets, it is observed clearly that the Pt/TiO_2 nanocrystals are wrapped by rGO sheets and the core-shell structure of $(\text{Pt}/\text{TiO}_2)@r\text{GO}$ catalysts is fabricated. For $(\text{Pt}/\text{TiO}_2)@r\text{GO-1}$ catalyst in Fig. 4c, Pt/TiO₂ nanocrystals are not wrapped completely owing to insufficient amount of wrapping rGO sheets. With increasing of rGO sheets, the uniform core-shell structure of $(\text{Pt}/\text{TiO}_2)@r\text{GO}$ catalysts is found. In Fig. 4d, it exhibited clearly the core-shell structure of Pt/TiO₂ nanocrystals wrapped by graphitic layers of rGO, and supported Pt NPs as intermedium are sandwiched between rGO shell and TiO₂ core. The thickness of rGO shell is in the range of 0.4–1.1 nm, which is equal to the thickness of 1–3 layers of single-layer rGO (0.34 nm) in inset of Fig. 4d. It is in accord with TEM images of $\text{TiO}_2@r\text{GO-2}$ catalyst in Fig. S5. After further increasing of wrapping rGO sheets, the thickness of rGO shell increases gradually, i.e., the average thicknesses of rGO shell over $(\text{Pt}/\text{TiO}_2)@r\text{GO-5}$ and $(\text{Pt}/\text{TiO}_2)@r\text{GO-10}$ catalysts are 2.5 and 5.0 nm, respectively.

The morphology and composition of $(\text{Pt}/\text{TiO}_2)@r\text{GO-2}$ catalyst were further characterized by the HAADF-STEM and EDS elemental mapping, and the result is shown in Fig. 4g. The four elements of Pt, O, Ti and C in the $(\text{Pt}/\text{TiO}_2)@r\text{GO-2}$ catalyst were detected by SEM-EDS spectroscopy (Fig. S6). Supported Pt NPs are homogeneously dispersed on the surface of TiO₂ supports, which is in agreement with the result of TEM images. The compositional distributions of each elements in the select local area of $(\text{Pt}/\text{TiO}_2)@r\text{GO-2}$ NPs reveal further obviously the tri-component core-shell-structured NPs with the core rich in Pt (sapphirine) and the shell rich in carbon (dark red), and Ti and O elements in the local area of Pt NPs are rare in comparison with surrounding. It indicates that Pt NP is deposited on the surface of TiO₂ and

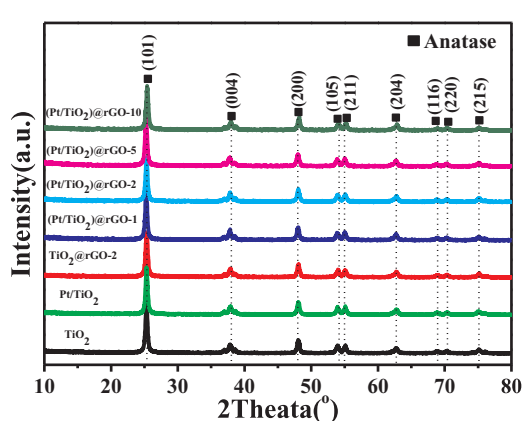


Fig. 2. XRD patterns of TiO_2 , Pt/TiO_2 , $\text{TiO}_2@r\text{GO-2}$ and $(\text{Pt}/\text{TiO}_2)@r\text{GO-n}$ catalysts.

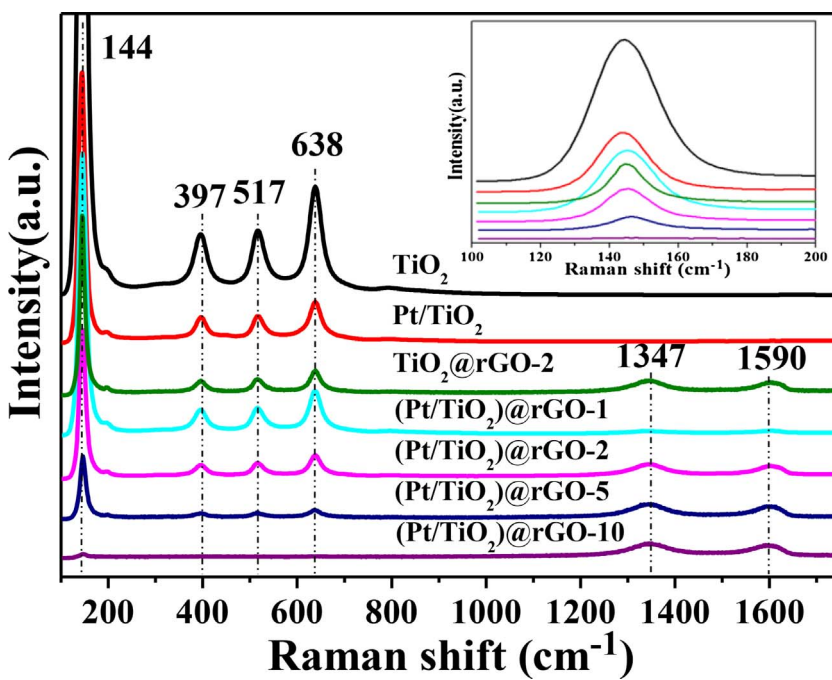


Fig. 3. Raman spectra of TiO_2 , Pt/TiO_2 , $\text{TiO}_2@\text{rGO-2}$ and $(\text{Pt}/\text{TiO}_2)@\text{rGO-n}$ catalysts.

subsequently is wrapped by rGO sheets. In other words, it is realized the formation of the core-shell structured $(\text{Pt}/\text{TiO}_2)@\text{rGO}$ catalysts. Therefore, a rGO(shell)-Pt(core)- TiO_2 (core) nanojunction system with a tight electronic contact ensures the efficient photogenerated electron transfer and the subsequent photocatalysis.

To examine the effect of core-shell structured (Pt/TiO_2) -rGO nanojunction on the electronic properties of the surface elemental (Ti, O, Pt and C), XPS spectroscopy was carried out and the results are shown in Fig. 5. As shown in Fig. 5a, the binding energies of $\text{Ti} 2p_{3/2}$ and $\text{Ti} 2p_{1/2}$ in TiO_2 nanocrystals are located at 457.8 and 463.5 eV, which is mainly assigned to Ti^{4+} species [54]. With increasing of rGO shell thickness in $(\text{Pt}/\text{TiO}_2)@\text{rGO-n}$ catalysts, the intensities of $\text{Ti} 2p$ XPS peaks decrease slightly, and the peaks have a positive shift gradually, which is attributed to the strong interactions of TiO_2 -Pt-rGO ternary system. For O1s XPS spectra in Fig. 5b, the curves exhibit one dominating peak at 528.8 eV and one secondary peak at 530.6 eV, which is ascribed to Ti–O bonding and surface O–H bonding of TiO_2 , respectively [55]. The deconvolution of O1s XPS spectrum of the $(\text{Pt}/\text{TiO}_2)@\text{rGO-2}$ catalyst obtained by the standard procedure is shown in Fig. S7. Four peaks of binding energies located at 529.1, 529.7, 530.8, and 531.8 eV have been fitted, which are ascribed to Ti–O–Ti (lattice O), C–O–Ti, Ti–OH, and C–OH (and C–O–C) species, respectively [56]. Being same as the $\text{Ti} 2p$ spectra, the Ti–O–Ti peaks for $(\text{Pt}/\text{TiO}_2)@\text{rGO}$ catalysts also have a positive shift in comparison with TiO_2 nanocrystals, which further proves the strong interactions and the electron transfer in the ternary system.

Fig. 5c shows Pt 4f XPS spectra of Pt/TiO_2 and $(\text{Pt}/\text{TiO}_2)@\text{rGO-n}$ catalysts. In order to observe clearly, the peak intensities of $(\text{Pt}/\text{TiO}_2)@\text{rGO-2}$ and $(\text{Pt}/\text{TiO}_2)@\text{rGO-10}$ catalysts are magnified to 1.5 and 2.0 times, respectively. After introduction of wrapping rGO sheets, the intensities of Pt 4f XPS peaks decrease obviously due to the shielding effect of rGO shell, which is also indirect evidence to the formation of $(\text{Pt}/\text{TiO}_2)@\text{rGO}$ core-shell structure. The deconvolutions of the spectra were made by the standard procedure, and the binding energies of 70.2 and 73.5 eV, 71.2 and 74.8 eV, 74.1 and 76.9 eV correspond to Pt^0 , Pt^{2+} and Pt^{4+} species, respectively. It indicates that the metallic (Pt^0) and ionic ($\text{Pt}^{&+}$) species coexist in $(\text{Pt}/\text{TiO}_2)@\text{rGO-n}$ catalysts. The formation of ionic $\text{Pt}^{&+}$ (Pt^{2+} and Pt^{4+}) species are derived from the electron transfer from Pt^0 to O^{2-} due to the strong interaction between metal (Pt)-support (rGO and TiO_2), which is beneficial to the vectorial

electron transfer from excitation of TiO_2 to rGO driven by the two steps using Pt NPs as conducting medium [57]. The relative proportions of Pt^0 , Pt^{2+} and Pt^{4+} species on the surface of catalysts were estimated and presented in Table 1. The surface $\text{Pt}^{&+}$ concentration of $(\text{Pt}/\text{TiO}_2)@\text{rGO-2}$ (47.1%) and $(\text{Pt}/\text{TiO}_2)@\text{rGO-10}$ (51.5%) catalysts are significantly higher than that of Pt/TiO_2 catalyst (29.9%), which is attributed to the strong electron transfer of $(\text{Pt}/\text{TiO}_2)@\text{rGO-n}$ core-shell catalyst from Pt NPs to rGO shell. Corresponding to the C 1s XPS spectra in Fig. 5d, the C 1s peak is dominated by elemental carbon at 283.9 eV, assigned mainly to the C–C, C=C and C–H bonds (sp^2) of graphene [58]. The other two peaks at 285.7 and 287.8 eV are assigned to the C–O and O=C=O species, respectively [59]. And the C 1s peak at ~ 281 eV corresponding to Ti–C bond is not observed, indicating that carbon atom did not directly enter into bulk TiO_2 lattice [60]. All of the element peaks are shifted to higher binding energy values than that for the pure TiO_2 , providing evidence of a strong interaction among rGO-Pt-TiO₂ ternary components, which is conducive to propelling the photogenerated electrons transfer from TiO_2 to rGO using Pt NPs as a medium.

In order to further observe the functional groups and chemical bonds of Ti–O–Ti vibrations and Ti–O–C vibrations, the Fourier transform infrared (FTIR) spectra of GO, TiO_2 and $(\text{Pt}/\text{TiO}_2)@\text{rGO-n}$ catalysts were investigated and the result is shown in Fig. 6. For comparison, the FTIR spectrum of GO is included. In the case of GO, there are five characteristic absorption bands in the region of 1000–3500 cm^{-1} . The absorption bands at 1048, 1392, 1628, 1726, and 3432 cm^{-1} were attributed to the C–O alkoxy, O=C–O carboxyl, C=C (skeleton of GO), C=O carbonyl and O–H stretching, respectively [61]. For pure TiO_2 , the spectrum shows a broad absorption peak around 500 cm^{-1} , which was attributed to the Ti–O–Ti stretching vibrations. The presence of absorption bands around 3400 and 1627 cm^{-1} were attributed to the O–H stretching frequency, which came from the surface hydroxyl groups and the adsorbed water molecules. For $(\text{Pt}/\text{TiO}_2)@\text{rGO-2}$ and $(\text{Pt}/\text{TiO}_2)@\text{rGO-10}$ catalysts, the intensity of absorption band at 1726 cm^{-1} corresponding to the oxygen functional groups decreased dramatically and even disappeared. The presence of absorption bands below 1000 cm^{-1} was attributed to the Ti–O–Ti and Ti–O–C stretching vibrations [62]. As a result, the chemically bond of Ti–O–C were formed by the residual carboxylic groups (COOH) on GO sheets interacted with the surface hydroxyl groups

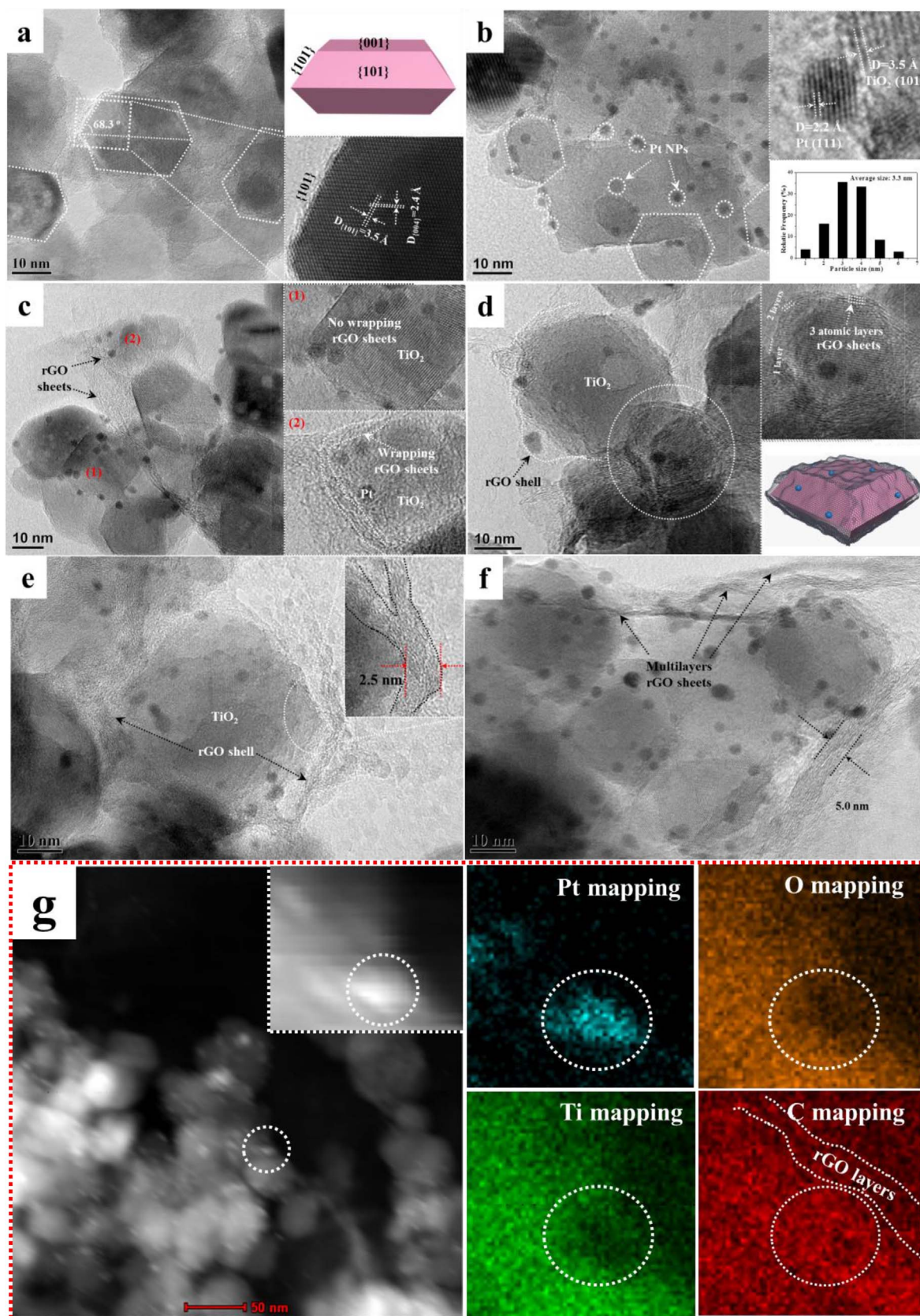


Fig. 4. TEM and HRTEM images of TiO_2 (a), Pt/TiO_2 (b), $(\text{Pt}/\text{TiO}_2)@\text{rGO-1}$ (c), $(\text{Pt}/\text{TiO}_2)@\text{rGO-2}$ (d), $(\text{Pt}/\text{TiO}_2)@\text{rGO-5}$ (e) and $(\text{Pt}/\text{TiO}_2)@\text{rGO-10}$ (f) catalysts. HAADF-STEM and EDS elemental mapping images of $(\text{Pt}/\text{TiO}_2)@\text{rGO-2}$ catalyst (g).

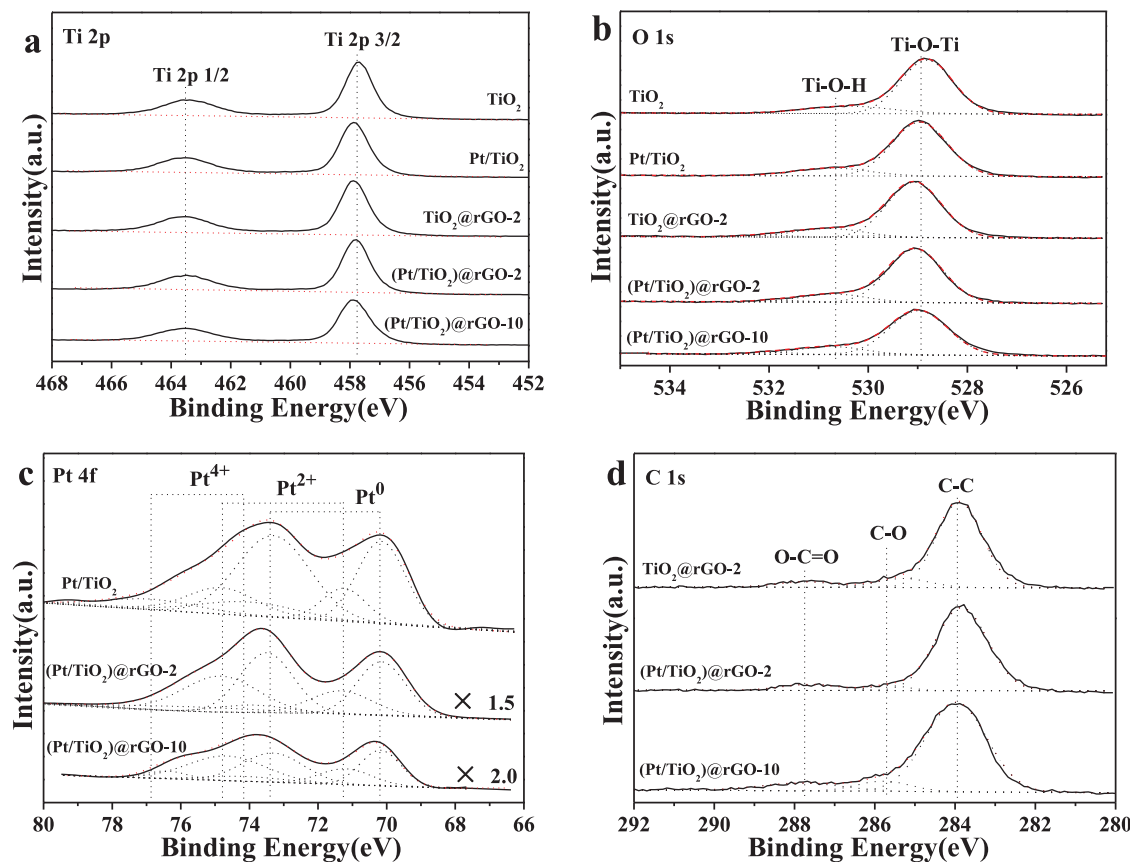


Fig. 5. XPS of Ti 2p (a), O 1s (b), Pt 4f (c) and C 1s (d) spectra of GO, TiO_2 , Pt/ TiO_2 , TiO_2 @rGO-2 and (Pt/ TiO_2)@rGO-n catalysts. For clear comparison, the XPS Pt 4f intensities of (Pt/ TiO_2)@rGO-2 and (Pt/ TiO_2)@rGO-10 in (c) are magnified to 1.5 and 2.0 times, respectively.

Table 1
Surface compositions and oxidation states of Pt species derived from XPS analyses.

Samples	Pt species (%)			
	Pt^0	Pt^{2+}	Pt^{4+}	$\text{Pt}^{&+}$ ^a
Pt/ TiO_2	70.1	20.3	9.6	29.9
(Pt/ TiO_2)@rGO-2	52.9	36.7	10.4	47.1
(Pt/ TiO_2)@rGO-10	48.5	40.1	11.4	51.5

^a The $\text{Pt}^{&+}$ values are equal to the sum of Pt^{2+} and Pt^{4+} .

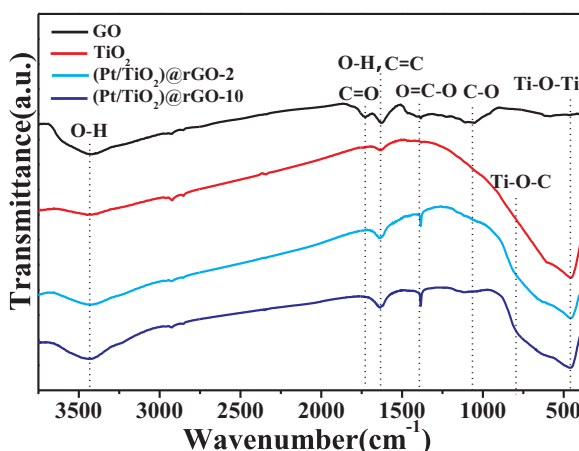


Fig. 6. FTIR spectra of GO, TiO_2 and (Pt/ TiO_2)@rGO-n catalysts.

(Ti—OH) of TiO_2 during mixing GO with TiO_2 nanocrystals. In addition, the intensity of Ti—O—Ti bands absorption band weakened obviously with the increasing of rGO content, which further confirmed that the rGO sheets wrapped on the surface of TiO_2 nanoparticles in accordance with the Raman, TEM and XRD results.

The optical absorption properties of TiO_2 , Pt/ TiO_2 and (Pt/ TiO_2)@rGO-n catalysts were investigated by means of UV-vis DRS and the result is shown in Fig. 7. For comparison, the commercial P25 is also included. Compared with limited visible light adsorption and wide band gap (~3.1 eV) of commercial P25, anatase TiO_2 nanocrystals show the strong absorption intensity in visible range, which is attributed to the existence of surface oxygen defects due to the presence of enlarged Ti—O—Ti bond angles and a mass of active unsaturated coordination Ti atoms on the {001} facet of anatase TiO_2 nanocrystals [63]. In order to elucidate relationship between the origin of visible absorption and oxygen defects, Fig. S8 shows the surface density of states (DOS) for $\text{TiO}_2(001)$ and $\text{TiO}_2(001)$ with an oxygen vacancy obtained by DFT calculation using VASP. TiO_2 with an oxygen vacancy (TiO_{2-x}) has one more peak near Fermi level compared with the stoichiometric TiO_2 , indicating that the surface of TiO_{2-x} is higher valence band energy level. Therefore, TiO_{2-x} needs lower energy to excite photogenerated electrons from valence band to conduction band. In other words, the photons in visible region can be absorbed by TiO_2 with an oxygen vacancy, but the stoichiometric TiO_2 cannot. Pt/ TiO_2 catalyst possesses stronger visible light absorption and displays a slight red shift of absorption edge compared with anatase TiO_2 nanocrystals, which is ascribed to the localized surface plasmon resonance effect of supported Pt NPs on enhanced light-trapping efficiency [64]. After further introduction of wrapping rGO sheets, the visible light absorption intensities of (Pt/ TiO_2)@rGO-n catalysts are improved, indicating that wrapping rGO sheets can enhance the visible light absorption efficiency. The band

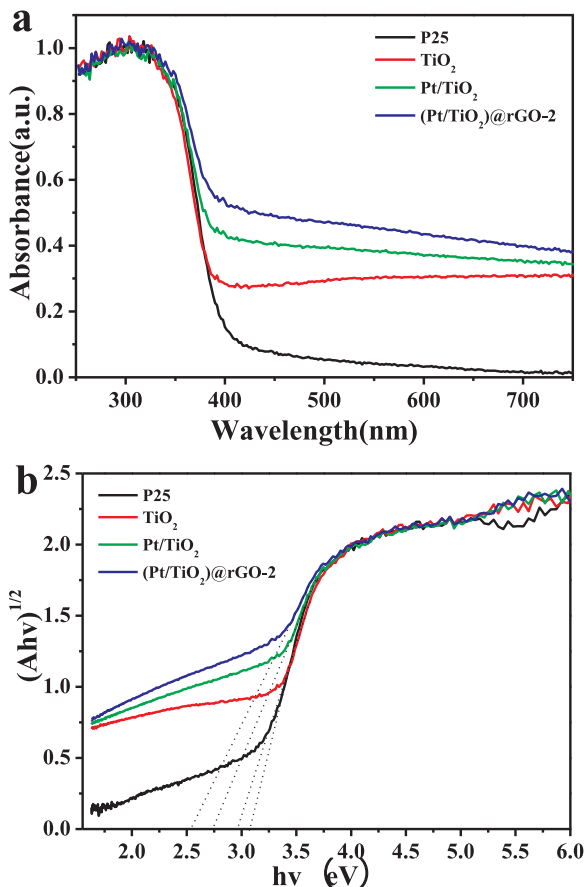


Fig. 7. UV-vis DRS (a) and Kubelka-Munk transformed reflectance spectra (b) of P25, TiO₂, Pt/TiO₂ and (Pt/TiO₂)@rGO-2 catalysts.

energy gap of samples could be calculated by the equation of $(\alpha h\nu)^n = A(h\nu - Eg)$, where α is the absorption coefficient, $h\nu$ is the absorption energy, A is the parameter that related to the effective masses associated with the valence and conduction bands, n is 1/2 for a direct transition and Eg is the band gap energy [65]. Fig. 7b shows the plotting $(\alpha h\nu)^{1/2}$ versus $h\nu$ based on the spectral response in Fig. 7a, and the extrapolated intercept corresponds to Eg values. It is noted that the Eg value (2.95 eV) of anatase TiO₂ nanocrystals is smaller than commercial P25 (3.10 eV). And the Eg value of Pt/TiO₂ catalyst is only 2.75 eV due to an additional absorption band of supported Pt NPs in the visible region. After introduction of Pt NPs and rGO sheets, (Pt/TiO₂)@rGO-2 catalyst shows the smallest optical band gap energy (2.55 eV), which is attributed to an additional absorption band of supported Pt NPs and rGO sheet in the visible region. Therefore, (Pt/TiO₂)@rGO-n catalysts with enhanced visible-light absorption are promising for photocatalytic reaction.

PL spectroscopy is a common method to understand the fate of photogenerated electron-hole pairs in semiconductor catalysts and it is quite helpful to explore the efficiency of the charge carrier separation, migration, trapping and recombination. The intensity of PL emission spectrum represents the recombination of photogenerated electrons and holes, and the lower intensity exhibits the less recombination of electrons and holes. Fig. 8 exhibits the PL spectra of P25, TiO₂, Pt/TiO₂, TiO₂@rGO-2 and (Pt/TiO₂)@rGO-n catalysts with the excitation wavelength of 380 nm. The emission peak centered at 390–550 nm is assigned to the emission of photogenerated electron-hole recombination. The PL emission intensity of anatase TiO₂ nanocrystals is lower than that of P25, indicating that the surface heterojunction between {001} and {101} facets in the single anatase TiO₂ nanocrystal can enhance transfer and separation of photogenerated electrons and holes. After

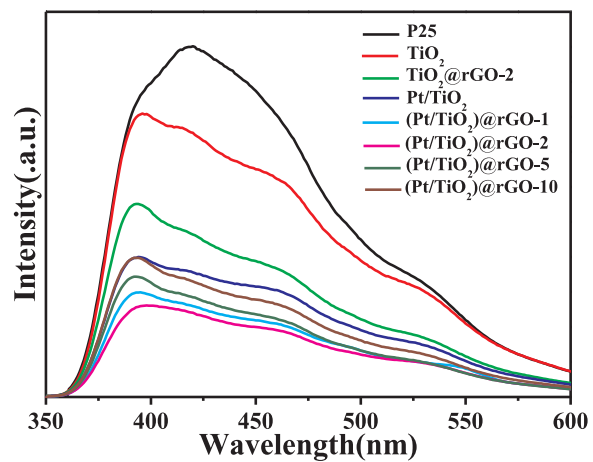


Fig. 8. Photoluminescence spectra ($\lambda_{\text{ex}} = 380$ nm) of P25, TiO₂, Pt/TiO₂, TiO₂@rGO-2 and (Pt/TiO₂)@rGO-n catalysts.

introduction of supported Pt NPs and wrapping rGO shell, the intensities of PL curves decrease successively, indicating that the ternary nanojunctions can diminish effectively the recombination of photogenerated charges and extend the life of photogenerated electrons, which is beneficial to improve the photocatalytic activity for CO₂ reduction. Among the prepared catalysts, (Pt/TiO₂)@rGO-2 catalyst exhibits the lowest intensity of PL emission spectra, indicating that the thickness of wrapping rGO sheets can optimize the recombination efficiency of photogenerated charges.

It is well known that the transient photocurrent response induced by the incident light can reflect the enrichment degree of separated charge carriers on the surface of photocatalysts [66]. The higher the photocurrent response is, the larger charge carrier number is [67]. In order to further illustrate the capability of supported Pt NPs and rGO shell for promoting separation efficiency of photoinduced electron-hole pairs in (Pt/TiO₂)@rGO photocatalysts, the transient photocurrent responses under several on/off UV-vis light irradiation cycles were performed, and the results are showed in Fig. 9. The photocurrent increased immediately when the light irradiation turns on, while it rapidly decreased to zero when the light turns off. The photocurrent density of anatase TiO₂ nanocrystals is higher than that of commercial P25, indicating the relatively high enrichment degree of photogenerated electrons due to the surface heterojunction effect between {001} and {101} facets. Moreover, the transient photocurrent intensities of bi-component Pt/TiO₂ and TiO₂@rGO-2 catalysts are higher than that of anatase TiO₂ nanocrystals, demonstrating that the photoinduced electrons and holes of Pt/TiO₂ and TiO₂@rGO catalysts prefer to separate

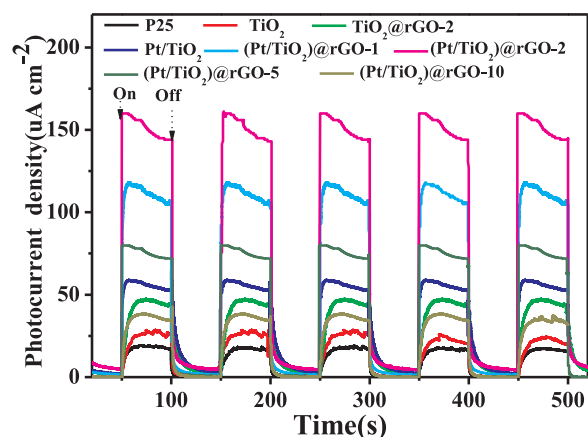


Fig. 9. Transient photocurrent responses of P25, TiO₂, Pt/TiO₂, TiO₂@rGO-2 and (Pt/TiO₂)@rGO-n catalysts.

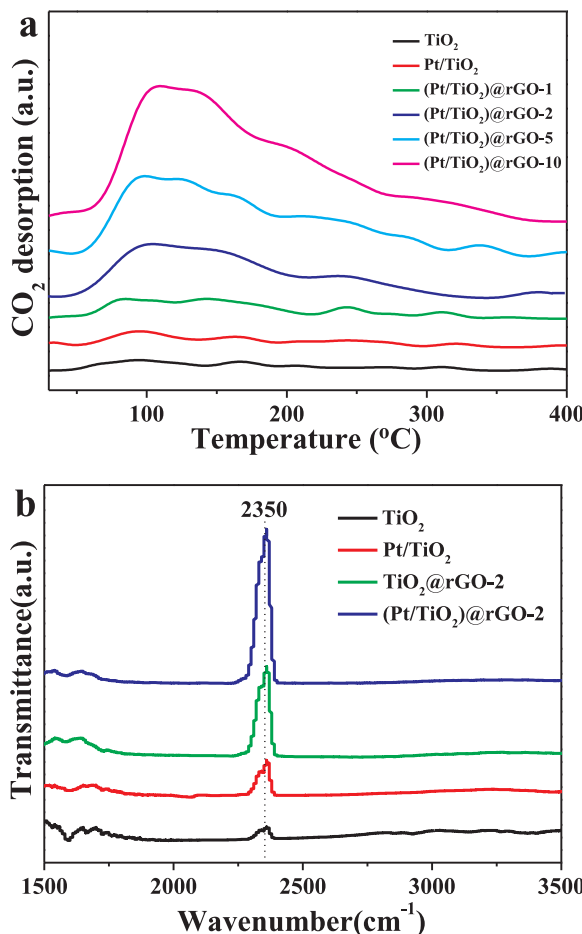


Fig. 10. Temperature-programmed desorption of CO₂ (CO₂-TPD) curves (a) and in-situ CO₂-adsorption DRIFTS spectra (b) of TiO₂, Pt/TiO₂, TiO₂@rGO-2 and (Pt/TiO₂)@rGO-n catalysts.

and transfer to surface rapidly. (Pt/TiO₂)@rGO-2 catalyst shows the highest photocurrent density, indicating that it has the most effective separation of the photogenerated charges and the highest surface enrichment degree of photogenerated electrons. The thickness of rGO shell can further optimize the separation efficiency of photogenerated electrons and holes, which is in consistent with the results of PL spectra. During five on/off cycles of light irradiation, all catalysts display a relatively stable photocurrent response, suggesting the good stability of photogenerated charges separation. All the observations with enhanced the separation of photogenerated electrons and holes highlight the excellent performance for photocatalytic reduction of CO₂ with H₂O.

The adsorption capacity for CO₂ reactant is also crucial to improve the catalytic activity. Fig. 10 shows the characterizations of CO₂-TPD and CO₂-adsorption DRIFTS spectra. As shown in Fig. 10a, the catalysts exhibit the desorption peak in the range of 70–180 and 180–350 °C, which is attributed to the strong physical adsorption and the weak chemical adsorption, respectively. The intensities of CO₂ desorption curves over (Pt/TiO₂)@rGO-n catalysts are higher than those of TiO₂ and Pt/TiO₂ catalysts, indicating the strong adsorption capacity for CO₂ reactant. With the increasing of wrapping rGO shell contents, the intensity of CO₂ desorption peaks increases remarkably. It indicates that wrapping rGO sheets can improve the adsorption performance of CO₂. The CO₂-adsorption DRIFTS spectra in Fig. 10b are further confirmed the results of enhanced adsorption capacity of wrapping rGO shell for CO₂ reactant. The peak at 2350 cm⁻¹ is attributed to the vibration of adsorbed CO₂ on the surface of catalysts. Among the catalysts, the peak intensity of (Pt/TiO₂)@rGO-2 catalyst is highest, and the peak intensities of TiO₂ and Pt/TiO₂ catalysts without rGO shells weaken

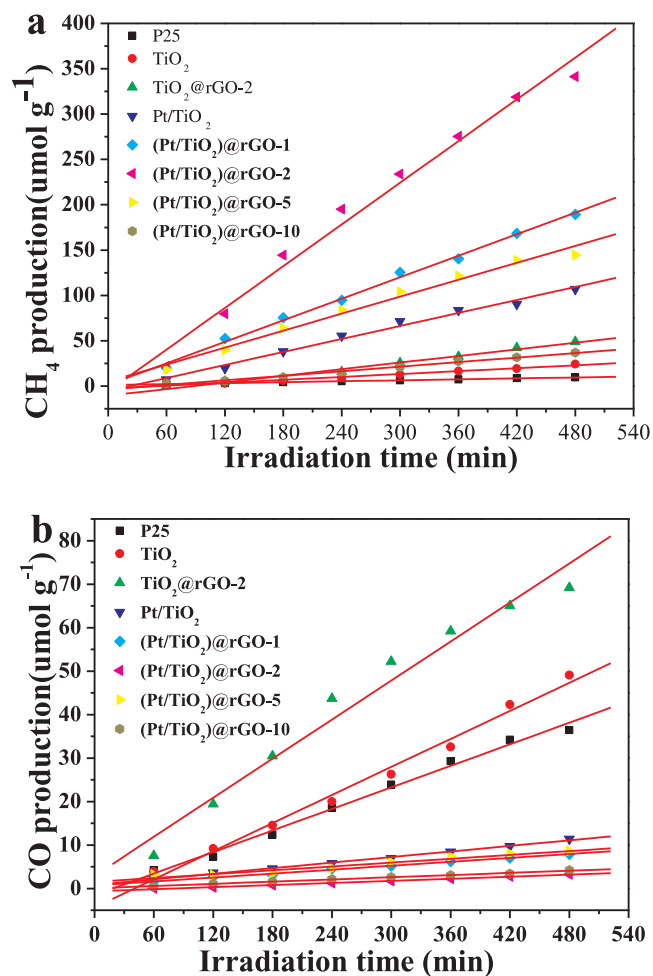


Fig. 11. Evolutions of CH₄ (a) and CO (b) productions for photocatalytic conversion of CO₂ with H₂O over TiO₂, Pt/TiO₂, TiO₂@rGO-2 and (Pt/TiO₂)@rGO-n catalysts.

distinctly. It indicates that the wrapping rGO shell can enhance the adsorption capacity of CO₂ reactant which is benefit for the conversion of CO₂ to CH₄. Based on the results of characterizations, (Pt/TiO₂)@rGO-2 catalyst, combined of both optimal photogenerated charges separation efficiency and maximal adsorption capacity for CO₂ reactant, is promising to exhibit the high photocatalytic activity for CO₂ reduction with H₂O to hydrocarbon fuels.

3.2. Photocatalytic activity for CO₂ reduction under simulated solar irradiation

The photocatalytic reduction of CO₂ with H₂O was carried out in a gas-closed circulation system with a continuous-flow mode under simulated light irradiation. Commercial P25 was selected as the reference catalyst in photocatalytic CO₂ reduction. The photocatalytic performances of as-prepared catalysts for CO₂ reduction with H₂O are shown in Fig. 11 and Table 2. As shown in Fig. 11, the product amounts of CH₄ and CO over anatase TiO₂ nanocrystals are larger than that of commercial P25. It is attributed to the surface heterojunction between co-exposed {101} and {001} facets in single anatase TiO₂ nanocrystals for improving the separation of photogenerated charges. The single co-catalysts of wrapping rGO sheets or supported Pt NPs can selectively improve the productive rate of CO and H₂, respectively. TiO₂@rGO-2 catalyst shows highest CO formation rate (8.6 μmol g⁻¹ h⁻¹), which is ascribed to the enhanced adsorption capacity for CO₂. Pt/TiO₂ catalyst exhibit the highest formation rate of H₂ (72.7 μmol g⁻¹ h⁻¹). It is attributed to the trapping photogenerated electrons of supported Pt NPs

Table 2

The formation rates, the selectivity of CO and CH₄ products and the apparent quantum efficiency (AQE) for photocatalytic conversion of CO₂ with H₂O over TiO₂, Pt/TiO₂, TiO₂@rGO-2 and (Pt/TiO₂)@rGO-n catalysts.

Sample	Formation rate [$\mu\text{mol g}^{-1} \text{h}^{-1}$] ^a				S _{CO} (%) ^b	S _{CH₄} (%) ^b	Selectivity for CO ₂ reduction (%) ^d	AQE Φ_{CH_4} (%) ^e
	CH ₄	CO	H ₂	O ₂				
P25	1.3	1.8	3.8	N.d. ^c	58.1	41.9	64.8	0.06
TiO ₂ -001/101	3.4	4.7	5.4	15.5	58.0	42.0	77.2	0.17
Pt/TiO ₂	13.3	1.3	72.7	67.3	7.0	93.0	42.8	0.65
TiO ₂ @rGO-2	6.0	8.6	0.8	17.7	58.9	41.1	95.5	0.30
(Pt/TiO ₂)@rGO-1	23.2	0.8	21.1	61.8	3.3	96.7	81.6	1.06
(Pt/TiO ₂)@rGO-2	41.3	0.4	5.6	98.4	0.9	99.1	96.7	1.93
(Pt/TiO ₂)@rGO-5	19.8	1.0	13.7	54.9	4.8	95.2	85.7	0.90
(Pt/TiO ₂)@rGO-10	4.7	0.4	3.7	12.0	7.8	92.2	83.8	0.25

^aReaction conditions: photocatalyst, 0.1 g; CO₂ pressure, 0.1 MPa; H₂O, 2.0 mL; light source, 320–780 nm; irradiation time, 8 h; reaction temperature, 4 °C.

^b Based on the ratio of [CO] or [CH₄] amounts to sum ([CO] + [CH₄]) amounts.

^c Not determined.

^d The selectivity was evaluated on an electron basis, equation: Selectivity (%) = [2n(CO) + 8n(CH₄)]/[2n(CO) + 8n(CH₄) + 2n(H₂)] × 100%.

^e The apparent quantum efficiency with irradiation light of 380 nm.

with the lower Fermi energy level. The increased electron density is beneficial to the formation of H₂ during the reaction process of consumption two electrons. Considering that the reduction of H₂O to H₂ is a competitive reaction with the reduction of CO₂ to CH₄ and CO, we have evaluated the selectivity for CO₂ reduction on an electron basis. It is noted that the photocatalytic selectivity to CO₂ reduction over Pt/TiO₂ catalyst is the lowest, and it increases obviously after wrapped rGO sheets. The selectivities of TiO₂@rGO and (Pt/TiO₂)@rGO-n catalysts for CO₂ reduction to CH₄ product are higher than 80%, indicating that wrapping rGO sheets are beneficial to the selective catalytic photoreduction of CO₂ with H₂O rather than H₂O reduction to H₂. Although rGO sheet is a more selective cocatalyst for the reduction of CO₂, the formation rate of CH₄ over TiO₂@rGO-2 is lower than that over Pt/TiO₂ catalyst, which may be attributed to the surface low density of photo-generated electrons without Pt NPs.

(Pt/TiO₂)@rGO-n catalysts exhibited a significantly enhancing photocatalytic activity for CO₂ reduction with H₂O to CH₄. Among the as-prepared catalysts, (Pt/TiO₂)@rGO-2 catalyst shows the highest formation rate of CH₄ (41.3 $\mu\text{mol g}^{-1} \text{h}^{-1}$) and the lowest formation rate of CO (0.4 $\mu\text{mol g}^{-1} \text{h}^{-1}$), its selectivity of CO₂ reduction to CH₄ product is 99.1%. The formation rate of CH₄ over (Pt/TiO₂)@rGO-2 catalyst has a 31-fold increase in comparison with commercial P25. It shows the noticeable synergistic effect of rGO-Pt-TiO₂ ternary system on enhancing the photocatalytic activity for CO₂ reduction. With increasing of wrapping rGO contents (> 2 wt%), the formation rate of CH₄ decreases remarkably and the selectivity for CO₂ reduction to CO product increases. It is attributed to increased shielding and scattering of photons through excess rGO in the photocatalytic system. Basis on the above results, the role of wrapping rGO shell can be summarized. On the one hand, the advantages of rGO shell are the enhanced adsorption capacity for CO₂ and separation efficiency of photogenerated electron-hole pairs. On the other hand, too much rGO shell can shield the light from reaching the surface of TiO₂ nanocrystals, which results in significant deterioration of photocatalytic performance for CO₂ reduction. Therefore, in order to achieve high efficient photocatalytic CO₂ reduction, the thickness of wrapping rGO shell must be optimized. Among the photocatalysts, (Pt/TiO₂)@rGO-2 catalyst showed the highest formation rate of CH₄, indicating that the weight percent (2 wt %) of wrapping rGO sheet is the optimum point between maximum positive and minimum negative effects. In addition, the formation rates of O₂ over the as-prepared catalysts were also investigated. In all the catalysts, (Pt/TiO₂)@rGO-2 catalyst shows the highest formation rate of O₂ (98.6 $\mu\text{mol g}^{-1} \text{h}^{-1}$) in Table 2, which is higher than the stoichiometric rate according to the calculation of CO₂ reduction products (85.6 $\mu\text{mol g}^{-1} \text{h}^{-1}$). It may be attributed to the formation of other undetected hydrocarbon. Therefore, it is concluded that the moderate

thickness of rGO shell on the surface of Pt/TiO₂-nanocrystals core is favorable to the photocatalytic CO₂ reduction with H₂O and can enhance the formation rate of CH₄.

The apparent quantum efficiency (AQE) is one of the most important parameters to light-chemical energy conversion. In the photocatalytic CO₂ reduction with H₂O reaction, the AQE values for CH₄ product (AQE_{CH₄}) over all catalysts were calculated by the equation in part 2.3, and the results are listed in Table 2. The AQE_{CH₄} value of anatase TiO₂ nanocrystals (0.17%) is higher than that of P25 (0.06%), indicating that anatase TiO₂ nanocrystal with coexposed {001} and {101} facets is a high efficiency photocatalytic system for CO₂ reduction to CH₄. The AQE_{CH₄} value of Pt/TiO₂ catalyst (0.65%) increases obviously compared with P25 and TiO₂. Among the (Pt/TiO₂)@rGO-n catalysts, (Pt/TiO₂)@rGO-2 catalyst exhibits the largest AQE_{CH₄} value (1.93%). It is further confirmed that the suitable thickness of rGO shells on the surface of Pt/TiO₂ nanocrystals is beneficial to improve the utilization efficiency of simulated solar irradiation. Fig. 12 shows the cycle test results of (Pt/TiO₂)@rGO-2 catalyst for CO₂ reduction. It exhibits excellent stability for photocatalytic CO₂ conversion, i.e., the formation rates of CH₄, CO and H₂ products have not changed obviously during the ten cycles. And the core-shell structure of (Pt/TiO₂)@rGO-n catalysts and the particle sizes of supported Pt NPs have not changed based on the results of SEM (Fig. S9a) and TEM (Fig. S9b) images. It indicates that (Pt/TiO₂)@rGO-n photocatalysts have a strong application potential for photocatalytic reduction of CO₂ with H₂O.

In addition, a series of background tests were also performed. Under conditions of simulated light irradiation without photocatalysts, any product of CO₂ conversion was not observed. Similarly, any hydrocarbon was not found under condition of without light even using (Pt/TiO₂)@rGO-2 catalyst.

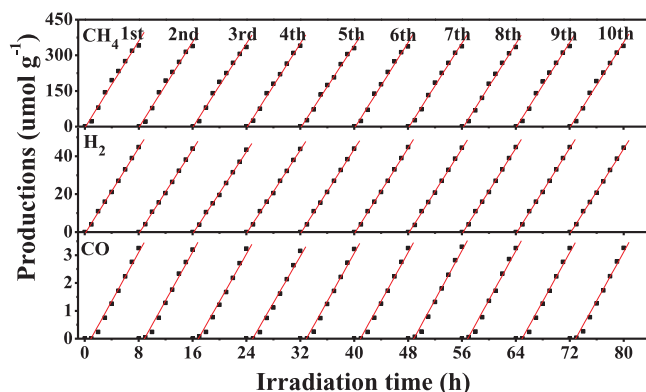


Fig. 12. Stability study on the formation rate of products (CH₄, CO and H₂) over (Pt/TiO₂)@rGO-2 catalyst for ten test cycles.

TiO_2)@rGO-2 photocatalyst. Using the feed gas of N_2 and H_2O vapor with (Pt/TiO_2) @rGO-n catalysts under simulated light irradiation, and again, the carbon-containing products were not detected. In order to verify the sources of carbon and hydrogen in the products of CO and CH_4 , the analyses of ^{13}C and $^2\text{H}(\text{D})$ isotopic tracing for the products of photocatalytic ^{13}C -labeled CO_2 reduction with D_2O over (Pt/TiO_2) @rGO-2 catalyst were carried out by means of GC-MS after 8 h irradiation (Fig. S10). The peak with m/z of 21 can be attributed to $^{13}\text{CD}_4$, and the peak with m/z of 29 can be recognized as ^{13}CO . It indicates that the carbon (C) element in the product of CO and CH_4 comes from CO_2 reactant, and the hydrogen (H) element in the product of CH_4 comes from H_2O reactant. Therefore, it is asserted that the reactants of CO_2 and H_2O are only source to photocatalytic products (CO and CH_4), both photocatalysts and light irradiation must be required for the reaction process of photocatalytic CO_2 reduction with H_2O .

4. Discussion

It is well known that the photocatalysts for CO_2 reduction must be confirmed to the energy band theory, which is based on the positions of oxidation potentials, conduction band (CB), and valence band (VB). The CB potential (E_{CB}) of TiO_2 (-0.56 V vs. NHE at pH 7) is more negative than the reduction potentials of $E^0(\text{CO}_2/\text{CO})$ (-0.53 V) and $E^0(\text{CO}_2/\text{CH}_4)$ (-0.24 V), so the reduction reaction is theoretically feasible. Although the $E^0(\text{CO}_2/\text{CH}_4)$ is less negative than $E^0(\text{CO}_2/\text{CO})$, but eight electrons are required to produce CH_4 rather than only two electrons for CO product [68]. Thus, the CO product is possible to be priority owing to the paucity of photogenerated electrons. But if the protons and electrons are sufficiently afforded during the photocatalytic process, CH_4 should be the major reduction product. Moreover, the basic process of photocatalytic CO_2 reduction can be summarized into three steps: 1) formation of photogenerated carriers (electron-hole pairs) by a band-gap excitation, 2) separation and transportation of the charge carriers, 3) reduction of water and carbon dioxide adsorbed on the surface of catalysts by the photogenerated electrons. Thus, the introduction of co-catalyst should be beneficial to improve the charge separation, facilitate the CO_2 adsorption and activation, and increase the catalytic active sites for the reduction process. Above all, the formation rate and selectivity of CH_4 products are dependent on the enrichment degree of electrons and reactants on the surface of photocatalysts, which is strongly related to the nanostructure and the surface property of photocatalysts.

Based on the results of photocatalytic CO_2 conversion with H_2O in Table 2, (Pt/TiO_2) @rGO-n catalysts exhibited super catalytic performances. The enhanced photocatalytic activity for CO_2 conversion with

H_2O can be isolated from light-harvesting, CO_2 adsorption and activation, and charge-separation functions of the photocatalysts. For improving the light-harvesting efficiency, the co-catalysts of supported Pt NPs and wrapping rGO sheets with the electronic coupling between π states of rGO and CB states of TiO_2 can effectively extend the spectral response from UV to visible region (Fig. 7). Based on comparison of the UV-vis DRS results between TiO_2 and (Pt/TiO_2) @rGO-2 catalysts, it is noted that the supported rGO sheets can further improve the absorption for visible light due to the electronic coupling between π states of rGO and conduction band states of TiO_2 . For enhancing CO_2 adsorption capacity, wrapping rGO sheets play the main role owing to their identical nonpolar property and abundant π electron cloud supported by the results of CO_2 -TPD and CO_2 -adsorption DRIFTS spectra (Fig. 10).

For effective separation efficiency of photogenerated charges, the rapid interfacial charge transfers from the surface heterojunction of {101} and {001} facets to Pt NPs and subsequent to rGO shell. Primarily, anatase TiO_2 nanocrystals are excited to produce electron-hole pairs by absorbed photons. The coexposed {101} and {001} facets of anatase TiO_2 nanocrystals can form a surface heterojunction, which is beneficial to effective separation of photogenerated electrons and holes. And then photogenerated electrons in the CB of TiO_2 transfer to supported Pt NPs. Combined the results of XPS (Fig. 5), PL (Fig. 8) and transient photocurrent (Fig. 9), the increasing of surface Pt^{4+} species has strong capacity to capture the electron from CB of TiO_2 . The supported Pt NPs in (Pt/TiO_2) @rGO-n catalysts are used as an accumulator and sensor for electron transfer in TiO_2 -Pt-rGO ternary system. And the photogenerated electrons can further transfer to rGO rather than stay in supported Pt NPs because of the strong electron withdrawing capacity of wrapping rGO shell, which can be illuminated by the increasing of Pt^{4+} species after introduction of rGO sheets. Thus, it occurs the vectorial electron transfer from TiO_2 to Pt NPs and even to rGO shell ($\text{TiO}_2 \rightarrow \text{Pt} \rightarrow \text{rGO}$). Finally, the photogenerated electrons are enriched on the tiny surface region of wrapping rGO shell, and subsequently react with the adsorbed CO_2 to CH_4 . In order to verify the vectorial electron transfer of $\text{TiO}_2 \rightarrow \text{Pt} \rightarrow \text{rGO}$, the experiment of Ag photodeposition on the surface of (Pt/TiO_2) @rGO-2 catalyst was carried out by irradiation with same light source of CO_2 reduction test for 30 min, and the results are shown in Fig. S11. The TEM images of Ag photodeposition over (Pt/TiO_2) @rGO-2 catalyst. Ag NPs with large sizes are almost deposited selectively on the surface of wrapping rGO shell and $\text{Ag}/(\text{Pt}/\text{TiO}_2)$ @rGO structure is formed. It indicates that the surface electron-rich region of wrapping rGO sheets is the active site of (Pt/TiO_2) @rGO-2 catalysts, which also proves the vectorial electron transfer of $\text{TiO}_2 \rightarrow \text{Pt} \rightarrow \text{rGO}$.

Based on the discussion above, the mechanism for the

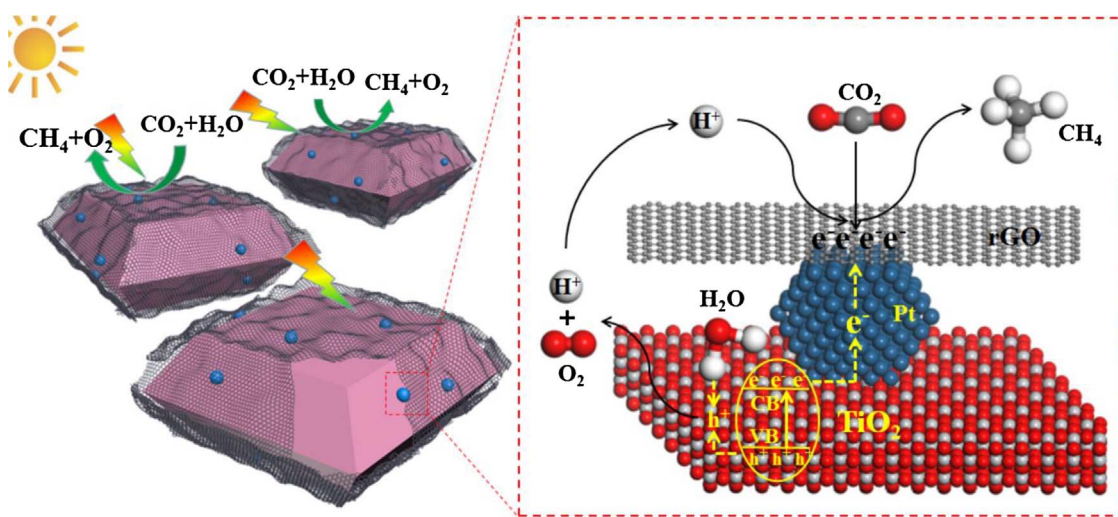


Fig. 13. Schematic of the mechanism for CO_2 photoreduction with H_2O to CH_4 over (Pt/TiO_2) @rGO-n catalysts.

photoreduction CO_2 with H_2O over $(\text{Pt}/\text{TiO}_2)@\text{rGO}$ catalysts is proposed and vividly shown in Fig. 13. In the rGO-Pt-TiO₂ ternary composites, anatase TiO₂ nanocrystals are the fountain of photogenerated electrons, and the coexposed {101} and {001} facets undertake a spade work for separation of electrons and holes. Supported Pt NPs act a key role to gather photogenerated electrons from the CB of anatase TiO₂ nanocrystal. And photogenerated electrons are enrichment on the tiny region of wrapping rGO shell via the vectorial electron transfer of $\text{TiO}_2 \rightarrow \text{Pt} \rightarrow \text{rGO}$. Ultimately, photogenerated electrons form an enriched region on the wrapping rGO shell, where CO_2 is reduced to CH_4 by the photogenerated electrons and H^+ . The holes left on the surface of TiO₂ nanocrystals can react with H_2O to O_2 accompanied by the generating of hydrogen ion for the consumption of CO_2 reduction. Meanwhile, the identical nonpolar property and abundant π electron cloud are conducive to the adsorption of CO_2 . This mechanism can ideally explain that the suitable thickness of rGO shells on the surface of Pt/TiO_2 is beneficial to CO_2 reduction and can enhance the formation rate of CH_4 except the influence from absorbance of rGO shells. The formation of rGO shells was incomplete with less content of rGO. And as mentioned earlier, too thick rGO shells can shield the light from reaching the surface of the TiO₂ photocatalyst and decrease the yield of photogenerated charges. There is a balance between the maximum positive and the minimum negative effects. Thus, the optimized rGO-Pt-TiO₂ ternary composites are beneficial to the multi-electron process of photocatalytic CO_2 conversion, and the unique electron collecting and transfer capabilities of rGO shell promote the selective production of CH_4 in photocatalytic CO_2 conversion. In other words, the vectorial electron transfer of $\text{TiO}_2 \rightarrow \text{Pt} \rightarrow \text{rGO}$ over the ternary composites system is beneficial to the separation of photogenerated electrons and holes, which can increase the formation rates and selectivity of CH_4 for CO_2 reduction. Therefore, $(\text{Pt}/\text{TiO}_2)@\text{rGO}$ catalysts, which takes all advantages of the high separation efficiency of photogenerated electrons and holes and the enhanced adsorption and activation capacities for CO_2 reactant, exhibited super photocatalytic performance for selective CO_2 conversion to CH_4 under the simulated solar irradiation.

5. Conclusions

We demonstrated a strategy to fabricate the novel core-shell-structured photocatalysts of Pt/TiO_2 nanocrystals wrapped by rGO sheets. Anatase TiO₂ nanocrystals with coexposed {001} and {101} facets can enhance the photogenerated charges separation efficiency preliminarily. Supported Pt NPs on the surface of TiO₂ nanocrystals are crucial to transfer and gather of photogenerated electrons for CO_2 conversion. The wrapping rGO sheets as an efficient electron acceptor and transporter are not only beneficial to enhance the enrichment of photogenerated electrons, but also their surface intrinsic hydroxyl and extended π bond are beneficial to enhance the adsorption and activation for CO_2 reactant. The rGO(shell)-Pt(medium)-TiO₂(core) ternary composites can promote the vectorial electron transfer of $\text{TiO}_2 \rightarrow \text{Pt} \rightarrow \text{rGO}$ and enhance photogenerated charges separation. $(\text{Pt}/\text{TiO}_2)@\text{rGO}$ -2 catalyst, which takes both advantages of the enhancing adsorption capacity of CO_2 reactants and the high separation efficiency of photogenerated electrons and holes, exhibited highest photocatalytic activity and selectivity for CO_2 conversion with H_2O to CH_4 under simulated solar irradiation, i.e., its formation rate of CH_4 ($41.3 \mu\text{mol g}^{-1} \text{h}^{-1}$) is about 31-fold of commercial P25 and the selectivity of CO_2 conversion to CH_4 product is closely to 100%. The innovative design and fabrication of $(\text{Pt}/\text{TiO}_2)@\text{rGO}$ photocatalysts, based on the aim of improving photogenerated charges separation and CO_2 adsorption capacity, are expected to be a new heuristic on the development of selectively photocatalytic CO_2 conversion to CH_4 .

Acknowledgements

We acknowledge the financial support from the National Natural

Science Foundation of China (21673142 and 21477164) and 863 Program of China (2015AA030903).

Appendix A. Supplementary data

Supplementary data associated with this article can be found, in the online version, at doi:10.1016/j.apcatb.2017.12.071.

References

- [1] A. Dhakshinamoorthy, S. Navalon, A. Corma, H. Garcia, Energy Environ. Sci. 5 (2012) 9217–9233.
- [2] F. Zuo, L. Wang, T. Wu, Z. Zhang, D. Borchardt, P. Feng, J. Am. Chem. Soc. 132 (2010) 11856.
- [3] X. Chang, T. Wang, J. Gong, Energy Environ. Sci. 7 (2016) 2177–2196.
- [4] E.V. Kondratenko, G. Mul, J. Balthusaitis, G.O. Larraábal, J. Perez-Ramirez, Energy Environ. Sci. 6 (2013) 3112–3135.
- [5] T. Inoue, A. Fujishima, S. Konishi, K. Honda, Nature 277 (1979) 637–638.
- [6] S. Sato, T. Morikawa, T. Kajino, O. Ishitani, Angew. Chem. Int. Ed. 52 (2013) 988–992.
- [7] Y. Bai, L. Ye, T. Chen, P. Wang, L. Wang, X. Shi, P.K. Wong, Appl. Catal. B 203 (2017) 633–640.
- [8] H. Liu, T.D. Dao, L. Liu, X. Meng, T. Nagao, J. Ye, Appl. Catal. B 209 (2017) 183–189.
- [9] S. Wang, X. Wang, Angew. Chem. Int. Ed. 55 (2016) 2308–2320.
- [10] M. Anpo, H. Yamashita, K. Ikeue, Y. Fujii, S.G. Zhang, Y. Ichihashi, D.R. Park, Y. Suzuki, K. Koyano, T. Tatsumi, Catal. Today 44 (1998) 327–332.
- [11] J. Jiao, Y. Wei, Z. Zhao, J. Liu, J. Li, A. Duan, G. Jiang, Ind. Eng. Chem. Res. 53 (2014) 17345–17354.
- [12] S. Wang, Y. Guan, L. Lu, Z. Shi, S. Yan, Z. Zou, Appl. Catal. B 224 (2018) 10–16.
- [13] T. Kamegawa, N. Suzuki, H. Yamashita, Energy Environ. Sci. 4 (2011) 14111–1416.
- [14] Y. Ma, X. Wang, Y. Jia, X. Chen, H. Han, C. Li, Chem. Rev. 114 (2014) 9987–10043.
- [15] Q. Zhang, T. Gao, J.M. Andino, Y. Li, Appl. Catal. B 123–124 (2012) 257–264.
- [16] Z. Bian, J. Zhu, J. Wen, F. Cao, Y. Huo, X. Qian, Y. Cao, M. Shen, H. Li, Y. Lu, Angew. Chem. Int. Ed. 50 (2011) 1105–1108.
- [17] X. Weng, Q. Zeng, Y. Zhang, F. Dong, Z. Wu, ACS Sustain. Chem. Eng. 4 (2016) 4314–4320.
- [18] W.J. Ong, L.L. Tan, S.P. Chai, S.T. Yong, A.R. Mohamed, Nanoscale 6 (2014) 1946–2008.
- [19] T. Tachikawa, S. Yamashita, T. Majima, J. Am. Chem. Soc. 133 (2011) 7197–7204.
- [20] J. Yu, J. Low, W. Xiao, P. Zhou, M. Jaroniec, J. Am. Chem. Soc. 136 (2014) 8839–8843.
- [21] Y. Cao, Q. Li, C. Li, J. Li, J. Yang, Appl. Catal. B 1 (198) (2016) 378–388.
- [22] S.N. Habersreuter, L. Schmidt-Mende, J.K. Stolarczyk, Angew. Chem. Int. Ed. 52 (2013) 7372–7408.
- [23] T.C. An, J.Y. Chen, X. Nie, G.Y. Li, H.M. Zhang, X.L. Liu, H.J. Zhao, ACS Appl. Mater. Interfaces 4 (2012) 5988–5996.
- [24] S. Bai, L. Wang, Z. Li, Y. Xiong, Adv. Sci. 4 (2017) 1600216.
- [25] Y. Wei, J. Jiao, Z. Zhao, W. Zhong, J. Li, J. Liu, G. Jiang, A. Duan, J. Mater. Chem. A 3 (2015) 11074–11085.
- [26] Q. Zhai, S. Xie, W. Fan, Q. Zhang, Y. Wang, W. Deng, Y. Wang, Angew. Chem. Int. Ed. 52 (2013) 5776–5779.
- [27] B. Cao, G. Li, H. Li, Appl. Catal. B 194 (2016) 42–49.
- [28] Z.Y. Zhang, S.W. Cao, Y.S. Liao, C. Xue, Appl. Catal. B 162 (2015) 204–209.
- [29] K. Ji, H. Dai, J. Deng, H. Zang, H. Arandiyani, S. Xie, H. Yang, Appl. Catal. B 168–169 (2015) 274–282.
- [30] F. Lin, D. Wang, Z. Jiang, Y. Ma, J. Li, R. Li, C. Li, Energy Environ. Sci. 5 (2012) 6400–6406.
- [31] F. Wang, Z. Jin, Y. Jiang, E.H.G. Backus, M. Bonn, S.N. Lou, D. Turchinovich, R. Amal, Appl. Catal. B 198 (2016) 25–31.
- [32] M.Q. Yang, Y. Zhang, N. Zhang, Z.R. Tang, Y.J. Xu, Sci. Rep. 3 (2013) 3314.
- [33] X. She, J. Wu, H. Xu, Z. Mo, J. Lian, Y. Song, L. Liu, D. Du, H. Li, Appl. Catal. B 202 (2017) 112–117.
- [34] Y. Li, W. Cui, L. Liu, R. Zong, W. Yao, Y. Liang, Y. Zhu, Appl. Catal. B 199 (2016) 412–423.
- [35] R. Long, N.J. English, O.V. Prezhdo, J. Am. Chem. Soc. 134 (2012) 14238–14248.
- [36] C. Dong, J. Lu, B. Qiu, B. Shen, M. Xing, J. Zhang, Appl. Catal. B 222 (2018) 146–156.
- [37] X. Bai, L. Wang, Y. Zhu, ACS Catal. 2 (2012) 2769–2778.
- [38] L. Zhang, H. Fu, Y. Zhu, Adv. Funct. Mater. 18 (2008) 2180–2189.
- [39] J. Chen, G. Li, Y. Huang, H. Zhang, H. Zhao, T. An, Appl. Catal. B 123–124 (2012) 69–77.
- [40] X.Y. Zhang, H.P. Li, X.L. Cui, Y.H. Lin, J. Mater. Chem. 20 (2010) 2801–2806.
- [41] M. Wang, J. Han, H. Xiong, R. Guo, Y. Yin, A.C.S. Appl. Mater. Interfaces 1 (7) (2015) 6909–6918.
- [42] X. Chen, Q. Chen, W. Jiang, Z. Wei, Y. Zhu, Appl. Catal. B 211 (2017) 106–113.
- [43] Z. Wang, S. Yan, Y. Sun, T. Xiong, F. Dong, W. Zhang, Appl. Catal. B 214 (2017) 148–157.
- [44] Y.T. Liang, B.K. Vijayan, K.A. Gray, M.C. Hersam, Nano Lett. 11 (2011) 2865–2870.
- [45] S.C. Cui, X.Z. Sun, J.G. Liu, ChemSusChem 9 (2016) 1698–1703.
- [46] L.L. Tan, W.J. Ong, S.P. Chai, A.R. Mohamed, Appl. Catal. B 166–167 (2015) 251–259.
- [47] X. Gong, W.Y. Teoh, J. Catal. 332 (2015) 101–111.

[48] S.D. Perera, R.G. Mariano, K. Vu, N. Nour, O. Seitz, Y. Chabal, K.J. Balkus Jr., *ACS Catal.* 2 (2012) 949–956.

[49] H.J. Shin, K.K. Kim, A. Benayad, S.M. Yoon, H.K. Park, I.S. Jung, M.H. Jin, H.K. Jeong, J.M. Kim, J.Y. Choi, Y.H. Lee, *Adv. Funct. Mater.* 19 (2009) 1987–1992.

[50] B.J. Morgan, G.W. Watson, *J. Phys. Chem. C* 113 (2009) 7322–7328.

[51] J. Jiao, Y. Wei, Y. Zhao, Z. Zhao, A. Duan, J. Liu, Y. Pang, J. Li, G. Jiang, Y. Wang, *Appl. Catal. B* 209 (2017) 228–239.

[52] H.G. Yang, C.H. Sun, S.Z. Qiao, J. Zou, G. Liu, S.C. Smith, H.M. Cheng, G.Q. Lu, *Nature* 453 (2008) 638–642.

[53] J. Zhu, S. Wang, Z. Bian, S. Xie, C. Cai, J. Wang, H. Yang, H. Li, *CrystEngComm* 12 (2010) 2219.

[54] G. Liu, H.G. Yang, X. Wang, L. Cheng, H. Lu, L. Wang, G.Q. Lu, H.M. Cheng, *J. Phys. Chem. C* 113 (2009) 21784–21788.

[55] Y. Luan, L. Jing, Y. Xie, X. Sun, Y. Feng, H. Fu, *ACS Catal.* 3 (2013) 1378–1385.

[56] B. Chai, T. Peng, J. Mao, K. Li, L. Zan, *Phys. Chem. Chem. Phys.* 14 (2012) 16745–16752.

[57] H. Tada, T. Mitsui, T. Kiyonaga, T. Akita, K. Tanaka, *Nat. Mater.* 5 (2006) 782.

[58] Y. Zhang, N. Zhang, Z.R. Tang, Y.J. Xu, *Phys. Chem. Chem. Phys.* 14 (2012) 9167–9175.

[59] E. Papirer, R. Lacroix, J.B. Donnet, G. Nansé, P. Fioux, *Carbon* 33 (1995) 63–72.

[60] W. Ren, Z. Ai, F. Jia, L. Zhang, X. Fan, Z. Zou, *Appl. Catal. B* 69 (2007) 138–144.

[61] J. Liu, H. Xu, Y. Xu, Y. Song, J. Lian, Y. Zhao, L. Wang, L. Huang, H. Ji, H. Li, *Appl. Catal. B* 207 (2017) 429–437.

[62] J. Liu, H. Bai, Y. Wang, Z. Liu, X. Zhang, D.D. Sun, *Adv. Funct. Mater.* 20 (2010) 4175–4181.

[63] L. Sun, Z. Zhao, Y. Zhou, L. Liu, *Nanoscale* 4 (2012) 613–620.

[64] J. Yu, L. Qi, M. Jaroniec, *J. Phys. Chem. C* 30 (2010) 13118–13125.

[65] Y. Wei, J. Jiao, Z. Zhao, J. Liu, J. Li, G. Jiang, Y. Wang, A. Duan, *Appl. Catal. B* 179 (2015) 422–432.

[66] W. Zhou, W. Li, J.Q. Wang, Y. Qu, Y. Yang, Y. Xie, K. Zhang, L. Wang, H. Fu, D. Zhao, *J. Am. Chem. Soc.* 136 (2014) 9280–9283.

[67] H. Zhang, X. Quan, S. Chen, H. Yu, N. Ma, *Chem. Mater.* 21 (2009) 3090–3095.

[68] J.L. White, M.F. Baruch, J.E. Pander III, Y. Hu, I.C. Fortmeyer, J.E. Park, T. Zhang, K. Liao, J. Gu, Y. Yan, T.W. Shaw, E. Abelev, A.B. Bocarsly, *Chem. Rev.* 115 (2015) 12888–12935.